Energy Advances

ROYAL SOCIETY OF CHEMISTRY

PAPER

View Article Online
View Journal | View Issue

Cite this: *Energy Adv.*, 2026, 5, 119

Factors controlling the performance of lithium-metal solid-state batteries with polyethylene oxide-based composite polymer electrolytes

Bapi Bera, Douglas S. Aaron and Matthew M. Mench *

Solid composite polymer electrolytes (CPEs) have emerged as a promising option due to their excellent ionic conductivity, mechanical flexibility, and compatibility with Li metal electrodes. In this study, polyethylene oxide (PEO) was selected as the base polymer, and a composite was formed with LLZTO and oxygen-vacancy LLZTO (OV-LLZTO) as an active ceramic filler. The surface defects in OV-LLZTO enhance its bonding with the PEO chains, leading to improved interfacial resistance, enhanced mechanical stability, prevention of PEO crystallization, mitigation of LLZTO nanoparticle agglomeration, and improved Li^+ ion conductivity. The removal of oxygen atoms from the LLZTO crystal results in lattice contraction, which strengthens the interaction between the LLZTO and PEO polymer chains, thereby reducing interfacial resistance and improving lithium-ion conductivity. In solid-state battery performance, the ionic conductivity and transference number of the solid electrolyte are crucial, along with thermal, mechanical, and electrochemical stability. While pristine PEO electrolytes exhibit higher conductivity than composites, they have a lower transference number and inferior stability compared to the composite electrolytes. As the temperature increases, the transference number of the polymer electrolyte increases due to increased ion mobility; however, with aging it decreases due to the formation of a passivation layer. A solid-state full cell employing the PEO/OV-LLZTO electrolyte was used to demonstrate high-rate capability (10C rate) and excellent capacity retention at 60 °C with a cathode areal loading of ~0.2 mAh cm^{-2}, underscoring its potential for high-performance battery applications.

Received 19th September 2025,
Accepted 24th November 2025

DOI: 10.1039/d5ya00278h

rsc.li/energy-advances

1. Introduction

The energy density of modern Li-ion batteries has reached a limit of approximately 300 Wh kg^{-1}.[1–3] One of the most straightforward approaches to enhance energy density is by replacing the conventional graphite anode with lithium metal.[4] However, lithium metal anodes suffer from challenges related to uneven plating and stripping, which contribute to capacity loss and the formation of dendrites. These dendrites can penetrate the separator, leading to internal short circuits and potential thermal runaway, especially since the conventional liquid electrolytes used in Li-ion batteries are highly flammable.[5–8] Solid-state batteries (SSBs) hold great promise for next-generation energy storage systems due to their potential to address safety concerns, increase energy density, and enable the use of high-energy electrode materials such as lithium (Li) metal.[9] Additionally, SSBs exhibit greater mechanical stability and can mitigate dendritic growth.[5] Furthermore, solid electrolytes show much higher thermal stability and have high durability, making the solid-state battery one of the best choices for the next generation of energy storage devices.

Researchers have been developing three major types of solid-state electrolytes for SSBs. The first one is solid ceramic-based electrolytes, which are mainly inorganic oxides ($La_3Li_7O_{12}Zr_2$ (LLZO), $Li_{6.4}La_3Zr_{1.4}Ta_{0.6}O_{12}$ (LLZTO), *etc.*), sulfides ($Li_{10}GeP_2S_{12}$ (LGPS)), phosphides, or halides.[10–12] This class has very good conductivity, as well as mechanical and thermal stability, but very high interfacial resistance and is difficult to manufacture.[12] The second type is based on organic polymers (*e.g.* polyethylene oxide (PEO), polyvinylidene fluoride (PVDF), polyacrylonitrile (PAN), poly(methyl methacrylate) (PMMA), *etc.*), which has very low interfacial resistance but tends to be electrochemically unstable.[13] Thirdly, composite polymer electrolytes (CPEs) are composites with soft base polymers and active ceramic fillers.[14–17] Among the various types of solid-state electrolytes, CPEs have emerged as a promising option owing to their excellent ionic conductivity, mechanical flexibility, and compatibility with Li metal electrodes.[18–24] Polyethylene oxide (PEO) polymer electrolytes

Department of Mechanical and Aerospace Engineering, University of Tennessee, Knoxville, USA. E-mail: mmench@utk.edu

have very good interfacial contact with electrodes due to their flexibility.[25] However, PEO is chemically and electrochemically unstable; a common solution is found in composite separators with solid ceramic additions. Such additions have been shown to enhance stability and conductivity and to improve physical properties.[26–32] Fu *et al.* reinforced surface defects on the LLZTO filler and prepared a composite electrolyte with PEO, which showed enhanced battery performance and high-rate capability.[5] The surface defects act as sites for PEO chains to attach, creating a strong polymer–ceramic interface. This bonding helps keep LLZTO particles well-dispersed, reduces PEO crystallization, and results in a uniform electrolyte with better strength, lower interfacial resistance, and higher Li^+ conductivity.

In this study, we investigate the factors influencing the performance of Li metal solid-state batteries utilizing composite polymer electrolytes. Our research focuses on elucidating key parameters that affect the electrochemical behavior and stability of these systems, aiming to enhance their overall performance and longevity. We explored PEO polymer and LLZTO ceramic fillers to enhance the electrolyte's mechanical strength, Li-ion conductivity, and interfacial stability with Li metal electrodes at 60 °C. As the conductivity and transference numbers are very low below 60 °C, all the experiments were carried at 60 °C, except the conductivity measurement (30 °C to 90 °C). The composite polymer electrolyte demonstrates better stability and high-rate capability compared to the baseline PEO membrane. Through this characterization study, insights into the design principles and optimization strategies for Li metal solid-state batteries employing CPEs are gained. Through systematic characterization techniques such as scanning electron microscopy (SEM), electrochemical impedance spectroscopy (EIS), and X-ray diffraction (XRD), insights into the microstructure and ion transport properties of the CPE are also gained.

2. Materials and methods

2.1 Materials

Poly(ethylene oxide) (PEO, MW 600k) and acetonitrile solvent were purchased from Sigma-Aldrich. Lithium bis(trifluoromethanesulfonyl)imide (LiTFSI), tantalum-doped LLZO powder ($Li_{6.4}La_3Zr_{1.4}Ta_{0.6}O_{12}$; particle size < 325 mesh, D50 ≈ 5 μm), 15 mm diameter Li-metal foil (0.5 mm thick), conductive carbon (Super P®), and polyvinylidene fluoride (PVDF) were purchased from MSE Supplies, USA. Lithium nickel–manganese–cobalt dioxide (NMC811) and lithium iron phosphate (LFP) cathode materials were purchased from MTI Corporation, USA.

The cathode (both LFP and NMC811) composition was 70 wt% active material with 10 wt% Super P® mixed with 20 wt% solid electrolyte binder (PEO and LiTSFI in acetonitrile solvent, 3 : 1 weight ratio), coated on an Al foil. The cathode was also cast without the solid electrolyte in the composition for comparison, establishing a baseline of PEO and LiTFSI. For this, the LFP cathode was prepared using 10 wt% PVDF binder and 80 wt% active material with 10 wt% Super P mixed with *N*-methyl-2-pyrrolidone (NMP) solvent and coated on an Al foil. The cathode areal loading was ∼0.2 mAh cm^{-2}.

2.2 Solid electrolyte synthesis

Oxygen vacancy LLZTO (OV-LLZTO) was synthesized *via* a custom thermal reduction method adapted from Fu *et al.*[5] Pristine LLZTO nanoparticles were heat-treated at 450 °C in a tube furnace for 10 h in a 5% H_2/argon atmosphere. The schematic of the synthesis procedure is shown in Fig. 1. The prepared OV-LLZTO was then transferred inside a glove box (Ar-gas filled).

2.3 Composite polymer electrolytes (CPEs) preparation

Composite polymer electrolytes (CPEs) were prepared at an EO : Li ratio of ∼12 with 32 wt% active filler. Specifically, 150 mg of LiTFSI, 270 mg of PEO (MW = 600 000) and 200 mg of LLZTO/OV-LLZTO were mixed in 6 ml of acetonitrile solvent for 24 h at 70 °C in a magnetic stirrer hot plate inside a glove box. Then the homogeneous mixture was poured in a Teflon™ Petri dish for 24 h at room temperature for drying in the antechamber of a glove box (O_2 < 0.1 ppm, H_2O < 0.1 ppm). A control separator did not have an active filler added to the PEO. After drying, the solid electrolyte was cut into 16 mm diameter discs, and for conductivity calculations an area of

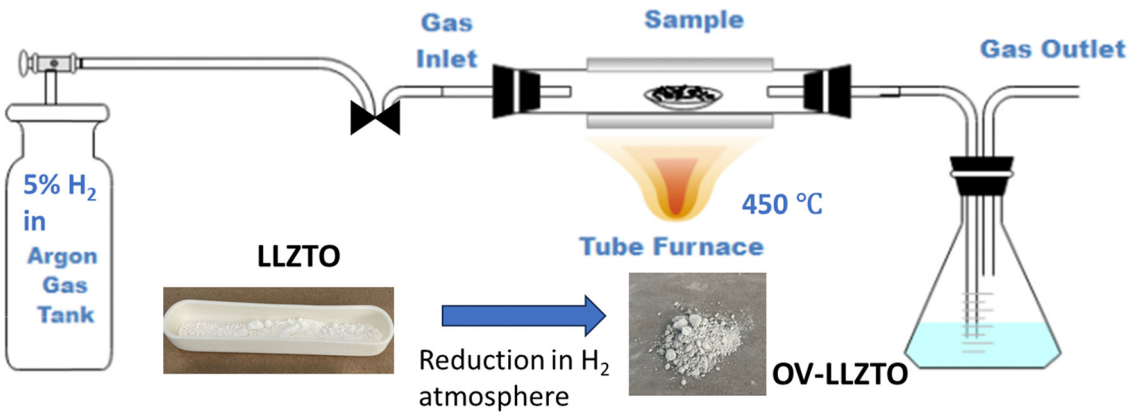

Fig. 1 Schematic of the synthesis procedure of OV-LLZTO.

1.7 cm^2 was used as the Li foil had a 15 mm diameter. The solid electrolyte thickness was in the ~90–110 μm range.

2.4 Physical characterization

The X-ray diffraction (XRD) patterns of the samples were obtained using a Panalytical Empyrean X-ray diffractometer (30 mA, 40 kV) with Cu Kα radiation (λ = 1.5406 Å). Data were collected over a 2θ range of 10° to 80° at a scanning speed of 10° min^{-1} with a step size of 0.01°. The surface morphology of PEO and composite PEO samples was characterized by high resolution scanning electron microscopy (SEM) on a Zeiss EVO instrument at 20 kV acceleration voltage and elemental analysis was carried out using energy dispersive X-ray spectroscopy (EDS) and X-ray photoelectron spectroscopy (XPS) for LLZTO and OV-LLZTO nanoparticles at the Institute for Advanced Materials and Manufacturing (IAMM, Knoxville, TN). Transmission electron microscopy (TEM) was carried out on a JEOL 1400 to analyze the LLZTO nanoparticle size before and after heat treatment at the Science and Engineering Research Facility (SERF, UTK). Thermal gravimetric analysis (TGA) and differential scanning calorimetry (DSC) were carried out using TA instruments Q-50 TGA and Q-2000 DSC, respectively. Stress and strain curves were measured using an Instron universal testing machine at a stretching speed of 0.1 mm min^{-1} at room temperature.

2.5 Electrochemical characterization

All-solid-state full-cell batteries were assembled using $LiFePO_4$ (LFP) or NMC 811 as the cathode material and lithium metal foil as the anode. The LFP-based cells were cycled between 2.5 and 4.0 V, while NMC 811 cells operated within a voltage range of 2.8–4.2 V (*vs.* Li/Li^+) at 60 °C, utilizing a Biologic BCS 815 cycler. *Ex situ* ionic conductivity was measured through electrochemical impedance spectroscopy (EIS) over a frequency range of 200 kHz to 0.1 Hz at temperatures ranging from 30 to 90 °C using a Biologic SP-150 instrument. The electrolyte was sandwiched between two stainless steel spacers for this measurement. The stability of the electrolyte against the lithium anode was assessed through galvanostatic cycling of Li–Li symmetric cells at different current densities. The measurements were conducted at 60 °C using a Biologic SP-150 instrument. The transference number indicates Li-ion conductivity through the solid separator and is an important indicator of the efficiency of the solid separator. The transference number was measured by chronoamperometry and EIS in the Li–Li symmetric cell. All the electrochemical measurement was carried in a coin cell CR2032 configuration. First, EIS was performed, and interfacial resistance was measured using equivalent circuit model fitting. Then, a 10 mV potential was applied to the symmetric cell for 1 h, followed by a second EIS measurement. The transference number was computed according to eqn (1):[33–35]

$$t^+ = \frac{I_{SS}(\Delta V - I_0 R_0)}{I_0(\Delta V - I_{SS} R_{SS})} \quad (1)$$

where I_0 and I_{SS} are the initial and steady state currents during the chronoamperometric experiment, ΔV is the polarization potential (10 mV), and R_0 and R_{SS} are the initial and steady state resistances collected by EIS. The transference number ranges between 0 and 1, with higher values indicating better lithium-ion transport and, consequently, improved performance. In Li-ion batteries, the transference number is generally higher compared to solid-state batteries (SSBs) due to more efficient lithium-ion diffusion in liquid electrolytes than in solid-state materials.

3. Results and discussion

LLZTO nanoparticles were heat-treated in an H_2 atmosphere to create oxygen atom vacancies in the lattice structure.[5] After reduction, white LLZTO becomes grayish in color. Removal of oxygen atoms causes a slight lattice contraction, which is reflected in both the XRD pattern and the binding-energy shifts observed in the XPS results. This observation ensures that oxygen vacancies are created in LLZTO nanoparticles.

Fig. 2(a) and (b) shows the TEM images of LLZTO nanoparticles and oxygen vacancy LLZTO (OV-LLZTO). From the TEM image, it was clear that there is no change in morphology, but the particle size reduces after H_2 reduction at high temperature. This may be due to the removal of oxygen atoms from the lattice, which reduces surface energy and induces lattice stress, promoting surface reconstruction or fragmentation of larger grains into smaller ones to minimize the total energy. Fig. 2(c) and (d) shows the SEM images of PEO and PEO/OV-LLZTO. The smooth surface of the electrolyte reduces the interfacial resistance of composite separators. Furthermore, the EDX spectra of PEO/OV-LLZTO shows uniform distribution of LLZTO nanoparticles in the PEO polymer matrix.

Fig. 3(a) shows the *in situ* high-temperature XRD pattern of PEO polymer electrolyte. At room temperature, PEO shows two crystallinity peaks at 2θ values of 18.5 and 23 degrees, corresponding to (120) and (112)/(032) planes, respectively.[36–38] Once the temperature reached 50 °C, the crystallinity of PEO vanished, and the film became amorphous. This amorphous state is better for Li-ion conductivity through the electrolyte. The XRD patterns of LLZTO and OV-LLZTO are shown in Fig. 3(b). The peak position of OV-LLZTO shifted to higher $2(\theta)$ values due to lattice contraction as oxygen atoms exited the crystal structure. The XRD patterns of the PEO polymer and composite electrolyte are shown in the SI (see Fig. S1). Results show that the crystallinity of LLZTO nanoparticles remains unchanged after composite formation with the PEO polymer. XPS measurements of LLZTO and oxygen-vacancy LLZTO nanoparticles were carried out and the results are shown in Fig. S2. The XPS results clearly show a significant binding energy shift after the introduction of oxygen vacancies in the LLZTO lattice.[5] The binding energy of O 1s becomes much lower after oxygen atom removal from the LLZTO lattice. Removal of oxygen creates oxygen vacancies, which act as electron donors in the lattice. The nearby metal cations (like Zr^{4+}, Ta^{5+}, and La^{3+}) become slightly more reduced (lower oxidation state). This increases the electron density around neighboring oxygen atoms. As a result, the

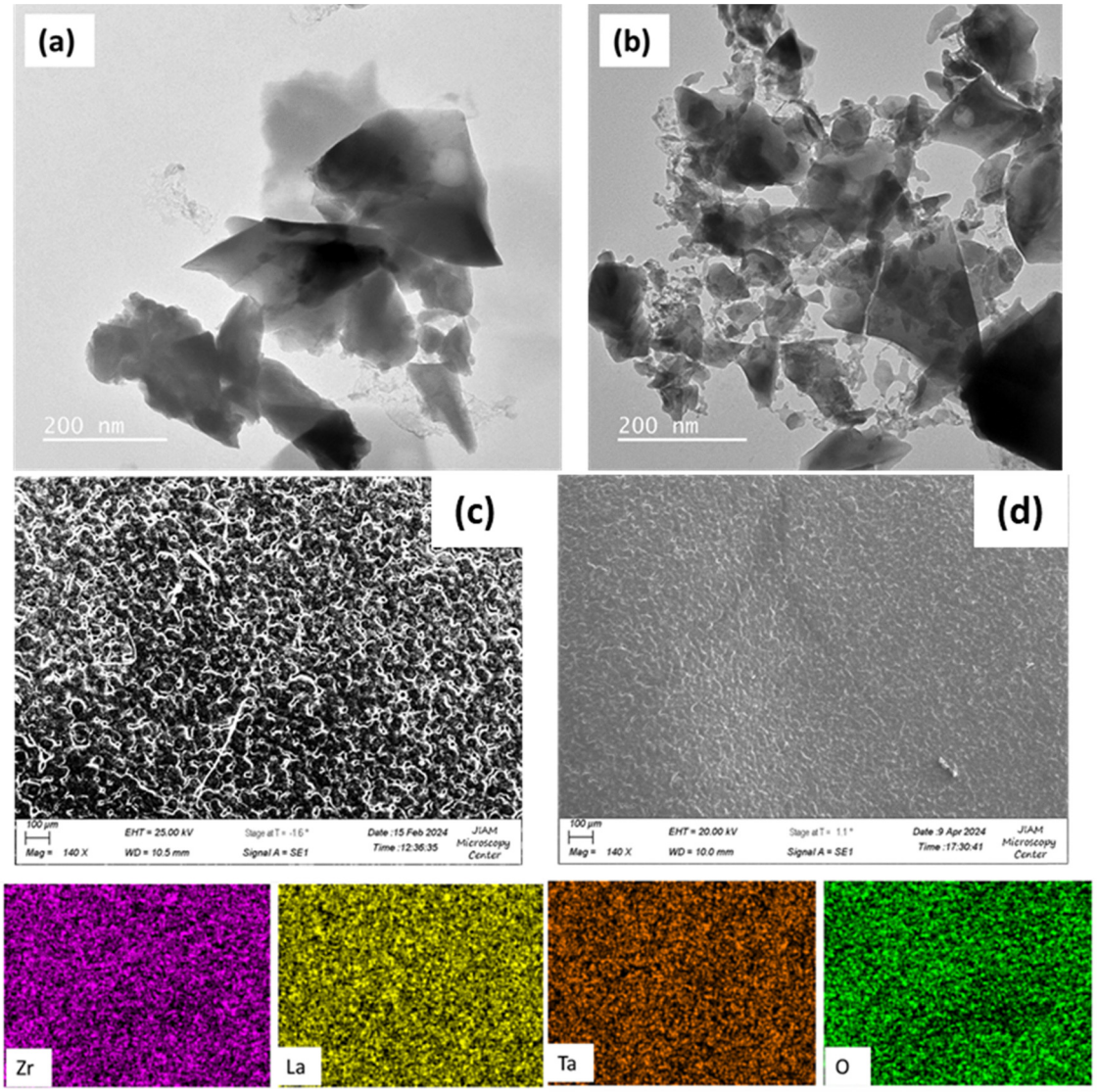

Fig. 2 TEM images of LLZTO (b) and OV-LLZTO (b). SEM images of (c) PEO and (d) PEO/OV-LLZTO. Bottom: EDX results of PEO/OV-LLZTO.

O 1s electrons are less tightly bound, so the binding energy decreases. Oxygen removal weakens the average M–O bond strength in the LLZTO lattice, which facilitates stronger bonding with oxygen atoms from PEO molecules, thereby reducing the interfacial resistance.

Fig. 3(c) shows the TGA profile of the PEO composite solid electrolyte. All the electrolytes are thermally stable up to 380 °C, but there is a small weight loss for PEO electrolyte at 100 °C. Due to the active filler in the composite electrolyte, the weight loss stops around 40%.[39] The DSC results of solid electrolyte (Fig. 3(d)) show the melting temperature of electrolytes decreasing after composite formation. The melting temperature is 51.2 °C for PEO, 48.6 °C for PEO/LLZTO, and 43.6 °C for PEO/OV-LLZTO.[40] After adding the active filler to the PEO membrane, the mechanical strength increases as shown in Fig. S3.[41]

Both conductivity and the transference number are crucial for the performance of solid-state batteries. However, the transference number holds greater significance than conductivity, as it specifically represents the fraction of current carried by Li^+ ions, whereas conductivity accounts for the current carried by all ions. Both parameters are highly temperature-dependent and tend to increase with increasing temperature. As a case study, the transference number of a PEO separator was measured at various temperatures to evaluate its performance.

Fig. 4(a) shows the Arrhenius plots of the measured σ against $1/T$ for membranes with three different solid electrolytes. As the temperature increases, conductivity increases due to the increase in the mobility of PEO chains, which enhances ion conduction.[42] At 60 °C, PEO shows higher conductivity than composite electrolytes. The conductivity of the solid electrolyte at 60 °C is shown in Table 1 and PEO has a conductivity of 0.52 mS cm^{-1}. Although the conductivity of PEO is higher compared to the composite, the full-cell performance was not optimal due to high voltage and current instability. Chronoamperometric

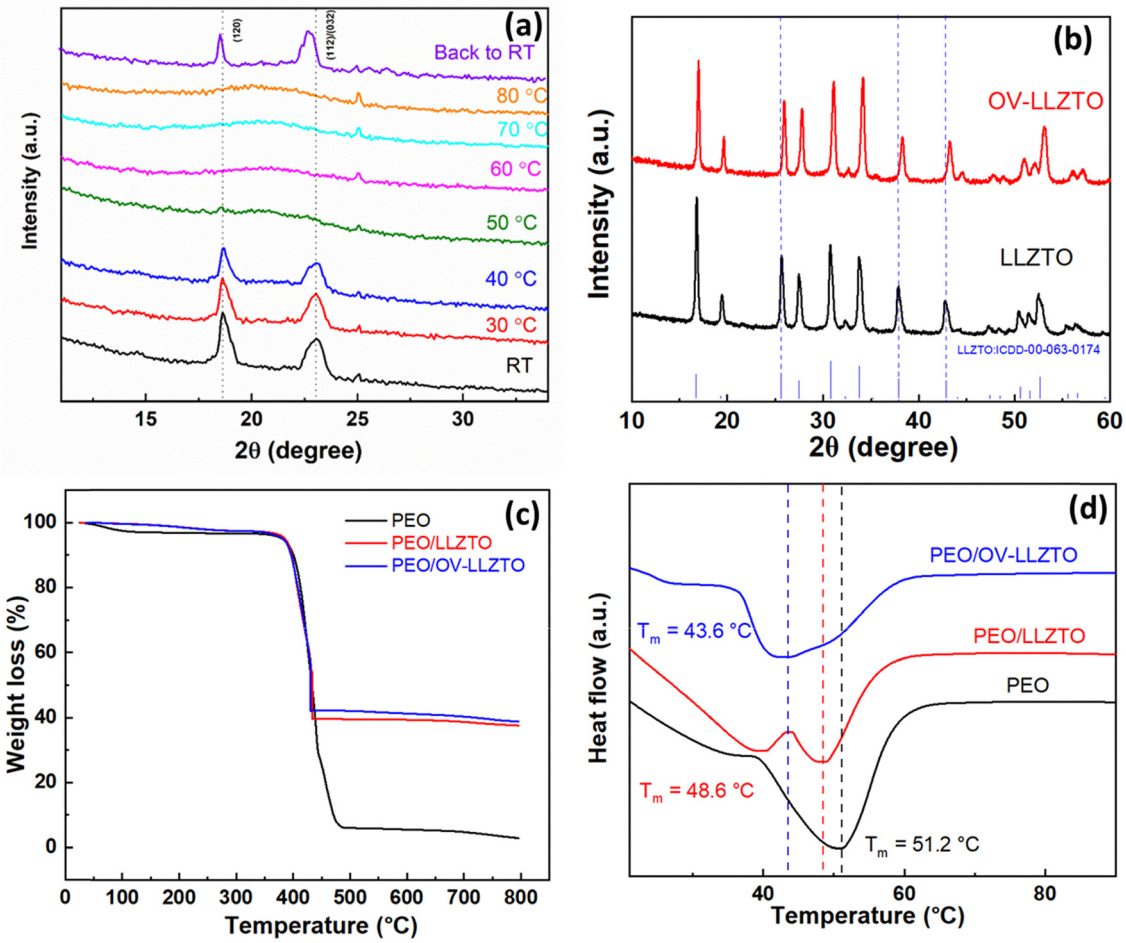

Fig. 3 (a) *In situ* temperature XRD pattern of PEO electrolyte. (b) XRD patterns of LLZTO and OV-LLZTO nanoparticles. (c) TGA profiles of the solid electrolyte. (d) DSC curves and the corresponding melting temperatures.

experiments of symmetric cells using different solid electrolytes at 10 mV polarization are shown in Fig. 4(b); all initially exhibited high current that stabilized within 750 s. PEO-LLZTO shows reduced current due to high resistance compared to PEO and PEO/OV-LLZTO. The resistance values from EIS measurements before and after polarization, as well as the steady state chronoamperometric current, are substituted in eqn (1) to obtain the transference number. Table 1 shows that PEO/OV-LLZTO has the highest transference number of ~0.31. Critical current was measured for all three solid electrolytes and is shown in Fig. S4. Critical current values are tabulated in Table 1 and for PEO/OV-LLZTO it was 0.8 mA.

Fig. 4(c) shows that the transference number increases with temperature for PEO solid electrolyte. As the temperature increases, the mobility of PEO chain molecules increases, and hence the transference number increases along with Li^+ ion conductivity. Transference numbers tend to decrease with aging due to passivation layer formation at each of the electrodes, as shown in Fig. 4(d).

Galvanostatic cycling of PEO/OV-LLZTO at ± 0.12 mA cm^{-2} current density is shown in Fig. 5(a). It shows constant voltage polarization with time for ~170 h. A lack of overpotential increase with cycling shows membrane stability in the electrochemical environment. Cycling was carried out until the cell short-circuited. The voltage interruption observed in Fig. 5(a) occurs because, during galvanostatic cycling at constant current, the experiment was paused after every 24 h of measurement. Chronoamperometry and electrochemical impedance spectroscopy (EIS) were then performed to evaluate the transference number and the evolution of charge-transfer resistance with aging. High frequency resistance (HFR) and charge-transfer resistance were measured from the EIS measurement, and the corresponding Nyquist plot is shown in Fig. S5. Initially, HFR decreased with cycling and then stabilized with time (see Fig. 5(b)). Charge-transfer resistance also decreases with time as shown in Fig. 5(c), which may be due to lithium plating on each of the electrodes, and with cycling the interface between the electrode and electrolyte gradually improves.[43] Though both HFR and charge transfer resistance decrease during cycling, overall cell polarization voltage does not reduce much as the transference number decreases with cycling (see Fig. 5(d)).

After full cell assembly with Li foil as the anode and LFP as the cathode, EIS was measured with three different solid

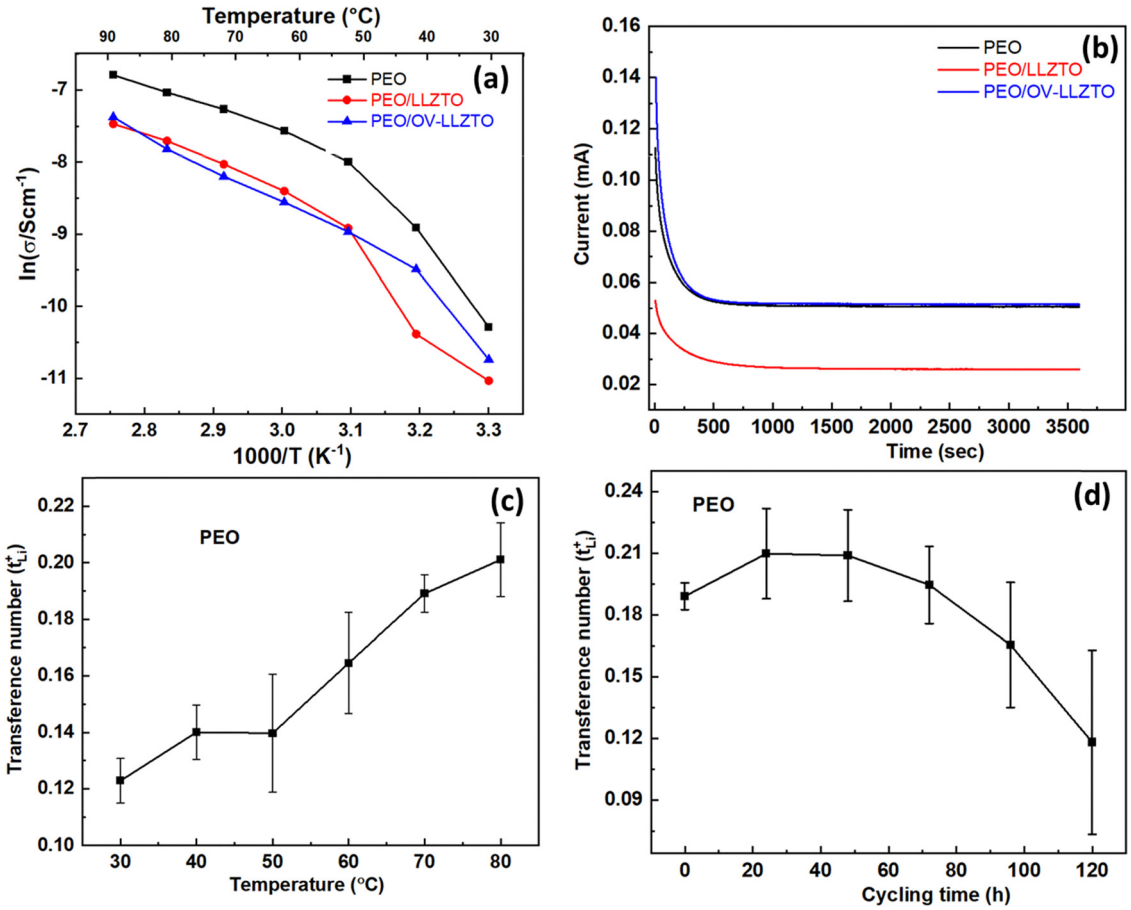

Fig. 4 (a) Arrhenius plots depicting the behavior of various electrolytes at different temperatures. (b) Current measurement with time at 10 mV polarization. Transference number with temperature (c) and aging (d).

Table 1 Summary of the beginning of life conductivity, transference number and critical current values for solid composite electrolytes at 60 °C

Electrolyte	Conductivity (mS cm^{-1})	Transference number	Critical current (mA)
PEO	0.52	0.23	0.5
PEO/LLZTO	0.23	0.21	0.7
PEO/OV-LLZTO	0.20	0.31	0.8

electrolytes and is shown in Fig. 6. EIS data were fitted with an equivalent circuit model (R1 + Q2/R2 + Q3), and HFR and charge-transfer resistance were measured. Both HFR and charge-transfer resistance increased when LLZTO nanoparticles were added in the PEO membrane (see Table 2). LLZTO nanoparticles increased the interfacial resistance and bad compatibility with both electrodes. When LLZTO reduces in an H_2 atmosphere and creates oxygen vacancies, it improves binding with PEO molecules, improving compatibility with solid electrolyte, enabling lower interfacial resistance and HFR.

Solid-state full cells were assembled with LFP and NMC811 cathodes and Li foil as the anode at 60 °C to evaluate the cell performance of the three solid electrolytes. Fig. 7(a) shows the charge–discharge profiles with different C rates from 0.25C to 10C for the PEO/OV-LLZTO solid separator using the LFP cathode. After 1C charge–discharge, the cell was cycled with 1C charge and a varying C rate discharge. The discharge capacity was relatively stable up to 3C discharge (decreasing from 160 mAh g^{-1} at 0.25C to 105 mAh g^{-1} at 3C). However, the increased discharge C rate to 5C and 10C led to larger losses in capacity. The rate capability of PEO/OV-LLZTO electrolyte under different C rates is plotted against the cycle number in Fig. 7(b). The full cell was cycled 210 times at different C rates. The first 50 cycles at a 0.25C rate established a nominal capacity of ~160 mAh g^{-1}; then, as the C rate increases, the capacity decreases. After the 1C charge–10C discharge step, the cell was again cycled at a 0.25C rate; the capacity returned to ~150 mAh g^{-1} but decayed relatively rapidly. This could be attributed to several factors arising during cycling at high C rate discharge, like lithium plating, electrode and electrolyte degradation, interfacial instability, *etc.*[44]

Similarly, full cells were assembled with the LFP cathode and the Li anode with PEO electrolyte and PEO/LLZTO electrolyte; the cycling performance of this cell is shown in Fig. S6 and S7 of the SI. The PEO separator shows a very low polarization voltage during charge–discharge tests, as well as comparable capacity at low C rates (0.25C), but does not cycle at high C rates

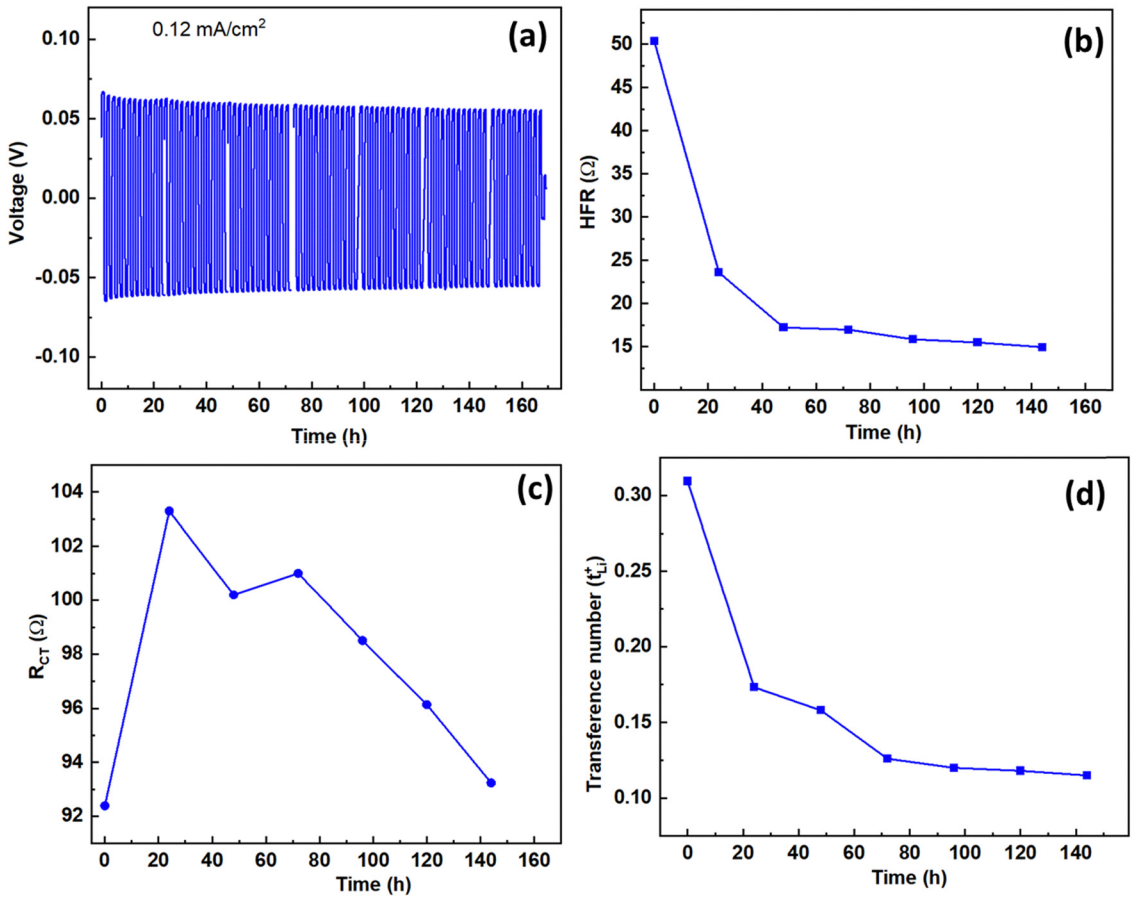

Fig. 5 (a) Galvanostatic cycling curves under 0.12 mA cm^{-2}; (b) HFR, (c) R_{CT}, and (d) transference number changes with cycling of PEO/OV-LLZTO electrolyte.

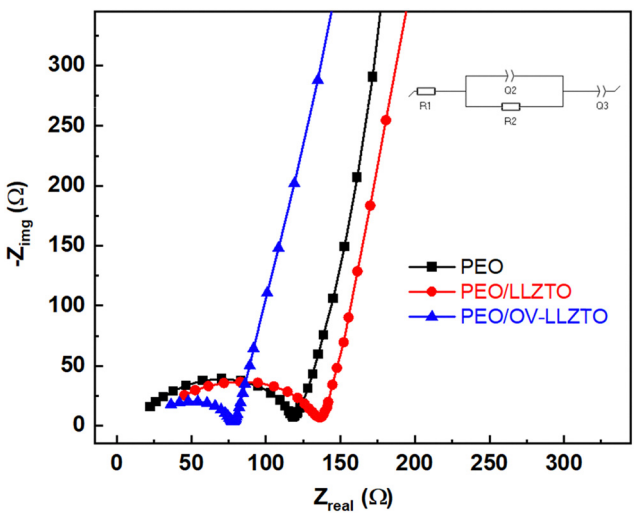

Fig. 6 EIS of all-solid-state LFP batteries with (a) PEO, (b) PEO/LLZTO and (c) PEO/OV-LLZTO after cell assembly.

above 0.5C. The initial cycling of the PEO/LFP cell shows a specific capacity of approximately 160 mAh g^{-1} at 0.25C and about 150 mAh g^{-1} at 0.5C. After 100 cycles, the capacity

Table 2 Resistances of the composite polymers after cell assembly at OCV

Samples	HFR (Ω)	Charge-transfer resistance (Ω)
PEO	13.5	109.8
PEO/LLZTO	23.8	115.2
PEO/OV-LLZTO	20.0	59.21

remains at 139 mAh g^{-1} at 0.25C, corresponding to a capacity retention of 87%. The PEO/LLZTO composite exhibits good rate capability but relatively low capacity, even at low C-rates. In contrast, the initial cycling of the PEO/LLZTO/LFP cell delivers a specific capacity of around 140 mAh g^{-1} at 0.25C. In all tests, PEO/LLZTO showed lower capacity during charge–discharge compared to PEO and PEO/OV-LLZTO electrolytes. EIS measurements were performed before and after cycling for each solid electrolyte, as shown in Fig. S8, and the corresponding results are summarized in Table ST1. The rate performance of the full cell using the NMC 811 cathode and PEO/OV-LLZTO electrolyte is shown in Fig. S9. The cell was cycled between 4.2 V and 2.8 V at different C rates. With cycling, the capacity decayed rapidly as the cell was operated at a high voltage, causing the PEO polymer electrolyte to decompose.

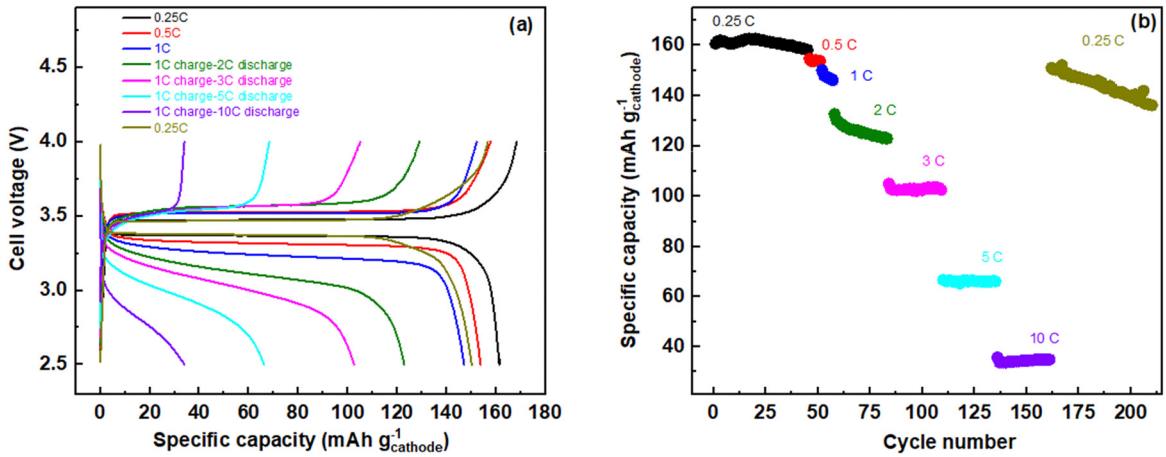

Fig. 7 (a) Rate performance of all-solid-state LFP battery with PEO/OV-LLZTO under different C-rates and (b) the corresponding capacity with the cycle number.

Fig. 8(a) shows the cyclic voltammograms (CVs) of the LFP cathode in three different electrolytes. The oxidation and reduction peaks of LFP are approximately symmetrical, indicating good reversibility of Li^+ extraction/insertion.[45] Peak-to-peak voltage separation for PEO (ΔV = 0.28 V) electrolyte is smaller than that for PEO/LLZTO (ΔV = 0.37 V) and PEO/OV-LLZTO (ΔV = 0.31 V) owing lower polarization and better reversibility.[45] Higher current for PEO electrolyte indicates better kinetics. Due to the better compatibility of PEO with solid electrode materials, Li^+ transport is very facile at the electrode–electrolyte interface, thus resulting in enhanced kinetics. But PEO is also unstable during charge–discharge cycling and at high voltage (>4.0 V).

EIS was conducted before and after CV, as shown in Fig. 8(b). There is an increase in charge-transfer resistance after cycling for all solid electrolytes due to passive layer formation at both the cathode and anode. When LLZTO ceramic is prepared as a composite with PEO, the interfacial resistance and charge transfer resistance increase; but both resistances decrease when OV-LLZTO was mixed with PEO polymer to prepare composite electrolyte. The CVs of the NMC 811 cathode in different solid electrolytes give distinct redox peaks appearing at different potential windows as shown in Fig. S10. These peaks emerged during the charging process due to multiple phase transitions, including hexagonal to monoclinic (H1→ M), monoclinic to hexagonal (M→ H2), and hexagonal to hexagonal (H2 → H3) transformations.[46–48] The oxidation current peak potentials corresponding to the hexagonal-to-monoclinic (H1→ M) phase transition were observed at 3.84 V for PEO, 3.86 V for PEO/LLZTO, and 3.83 V for PEO/OV-LLZTO electrolytes.[47] These CV results indicate that the PEO/OV-LLZTO electrolyte reduces overpotential compared to PEO and PEO/LLZTO.

To understand the effect of solid electrolyte incorporation into cathode materials, an LFP cathode was prepared without adding a solid electrolyte. A full cell consisting of the LFP cathode (without solid polymer electrolyte) and a lithium metal anode was cycled at a 0.2C rate for 100 cycles at 60 °C, as shown in Fig. S11. Initially, the capacity was low, but it increased with cycling, indicating that the presence of a solid electrolyte in the

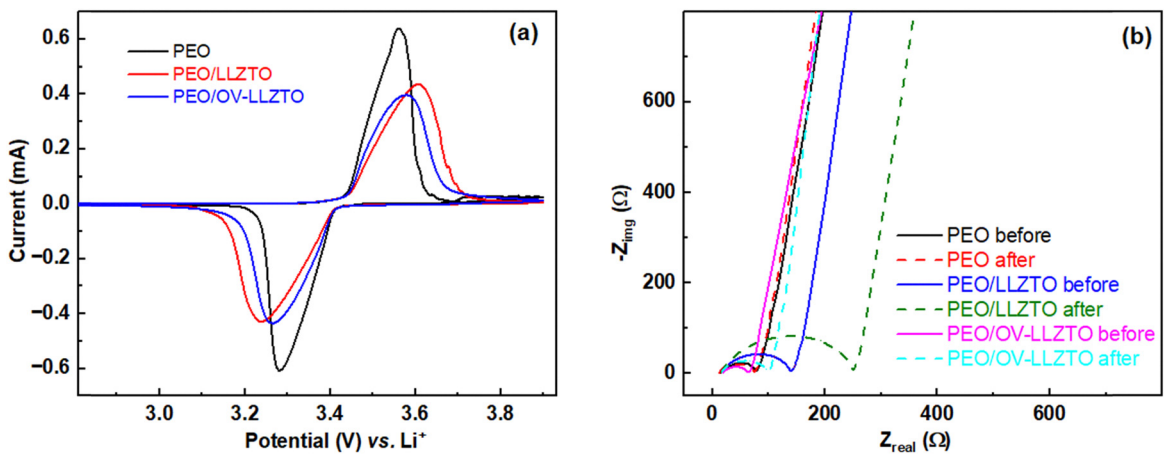

Fig. 8 Cyclic voltammograms of LFP (a) in three different solid electrolytes. EIS curves of the LFP cathode before and after cycling (b).

cathode is essential for improved performance during initial cycling.

4. Conclusions

In summary, a composite solid electrolyte (PEO/OV-LLZTO) for solid-state batteries was prepared and evaluated. A full cell made with Li metal as the anode and an LFP cathode with composite electrolyte shows good capacity and rate capability (up to 10C rate) at 60 °C. The performance of solid-state batteries is influenced not only by the ionic conductivity of the electrolyte but also by the transference number, which plays a crucial role in determining the efficiency of lithium-ion transport. While PEO electrolytes exhibit higher conductivity compared to composite electrolytes, they demonstrate a lower transference number, which may limit overall battery performance. However, as the temperature increases, the transference number of polymer electrolytes improves due to enhanced ion mobility, though aging can lead to a decline in performance due to passivation layer formation.

Achieving low interfacial resistance between the solid electrolyte and electrode materials is key to ensuring stability and enhancing battery performance. Incorporating polymers into the cathode material's composition has been found to reduce this interfacial resistance. The removal of oxygen atoms in LLZTO leads to lattice contraction, as observed through XRD and TEM analyses. This lattice contraction facilitates stronger bonding between LLZTO and the PEO polymer chains, reducing interfacial resistance and improving lithium-ion conductivity. Therefore, optimizing the electrolyte's transference number, managing interfacial resistance, and fine-tuning material compositions are essential to advancing solid-state battery technology.

Improving the ionic conductivity of solid electrolytes remains critical for practical lithium-metal solid-state batteries, especially at room temperature. Future efforts should focus on optimizing polymer–ceramic interfaces, introducing controlled defects, and refining composite structures to enhance Li^+ transport and long-term stability.

Author contributions

Bapi Bera: methodology, validation, formal analysis, investigation, data curation, conceptualization, writing – original draft, visualization. Douglas S. Aaron: project administration, funding acquisition. Matthew M. Mench: writing – review & editing, resources, project administration, funding acquisition.

Conflicts of interest

The authors declare that they have no known competing financial interests or personal relationships that could have appeared to influence the work reported in this paper.

Data availability

Physical characterization data, including stress measurements, XRD, and XPS, as well as electrochemical data, including cyclic voltammograms, EIS, and charge–discharge cycling results, are provided in the supplementary information and will also be available from the authors upon reasonable request.

The data supporting this article have been included as part of the supplementary information (SI). Supplementary information (SI) is available. See DOI: https://doi.org/10.1039/d5ya00278h.

Acknowledgements

This research was supported by the Army Research Laboratory under Cooperative Agreement Number W911NF2220007. The findings and conclusions presented in this document reflect the views of the authors and should not be construed as the official stance, whether stated or implied, of the Army Research Office or the U.S. Government. Regardless of any copyright notices herein, the U.S. Government retains the right to reproduce and distribute reprints for governmental purposes. The authors extend their gratitude to the Institute for Advanced Materials and Manufacturing (IAMM) and the Department of Mechanical, Aerospace, and Biomedical Engineering at The University of Tennessee, Knoxville, USA, for their support.

References

1 F. Lv, Z. Wang, L. Shi, J. Zhu, K. Edstrom, J. Mindemark and S. Yuan, Challenges and development of composite solid-state electrolytes for high-performance lithium-ion batteries, *J. Power Sources*, 2019, **441**, 227175.
2 S. Zhang, K. Ueno, K. Dokko and M. Watanabe, Recent Advances in Electrolytes for Lithium–Sulfur Batteries, *Adv. Energy Mater.*, 2015, **5**, 1500117.
3 B. Bera, A. Roy, D. Aaron and M. M. Mench, Understanding the Transport Phenomena in Solid State Battery (SSB), *Electrochem. Soc. Meet. Abst.-241*, 2022, **1**, 45.
4 C. Martin, M. Genovese, A. J. Louli, R. Weber and J. R. Dahn, Cycling Lithium Metal on Graphite to Form Hybrid Lithium-Ion/Lithium Metal Cells, *Joule*, 2020, **4**, 1296–1310.
5 Y. Fu, K. Yang, S. Xue, W. Li, S. Chen, Y. Song, Z. Song, W. Zhao, Y. Zhao, F. Pan, L. Yang and X. Sun, Surface Defects Reinforced Polymer-Ceramic Interfacial Anchoring for High-Rate Flexible Solid-State Batteries, *Adv. Funct. Mater.*, 2023, **33**, 2210845.
6 L.-Z. Fan, H. He and C.-W. Nan, Tailoring inorganic–polymer composites for the mass production of solid-state batteries, *Nat. Rev.*, 2021, **6**, 1003.
7 W. Li, E. M. Erickson and A. Manthiram, High-nickel layered oxide cathodes for lithium-based automotive batteries, *Nat. Energy*, 2020, **5**, 26–34.
8 J. B. Goodenough and K.-S. Park, The Li-Ion Rechargeable Battery: A Perspective, *J. Am. Chem. Soc.*, 2013, **135**, 1167–1176.

9 S. K. Sharma, G. Sharma, A. Gaur, A. Arya, F. S. Mirsafi, R. Abolhassani, H.-G. Rubahn, J.-S. Yu and Y. K. Mishra, Progress in electrode and electrolyte materials: path to all-solid-state Li-ion batteries, *Energy Adv.*, 2022, **1**, 457.

10 W. Lan, H. Fan, V. W. Lau, J. Zhang, J. Zhang and R. Zhao, and Hongyu Chen, Realizing $Li_7La_3Zr_2O_{12}$ garnets with high Li^+ conductivity and dense microstructures by Ga/Nb dual substitution for lithium solid-state battery applications, *Sustainable Energy Fuels*, 2020, **4**, 1812.

11 M.-J. Kim, I.-H. Choi, S. C. Jo, B. G. Kim, Y.-C. Ha, S.-M. Lee, S. Kang, K.-J. Baeg and J.-W. Park, A Novel Strategy to Overcome the Hurdle for Commercial All-Solid-State Batteries via Low-Cost Synthesis of Sulfide Solid Electrolytes, *Small Methods*, 2021, **5**, 2100793.

12 H. Kwak, S. Wang, J. Park, Y. Liu, K. T. Kim, Y. Choi, Y. Mo and Y. S. Jung, Emerging Halide Superionic Conductors for All-Solid-State Batteries: Design, Synthesis, and Practical Applications, *ACS Energy Lett.*, 2022, **7**, 1776.

13 J. Shi, Y. Yang and H. Shao, Co-polymerization and blending based PEO/PMMA/P(VDF HFP) gel polymer electrolyte for rechargeable lithium metal batteries, *J. Membr. Sci.*, 2018, **547**, 1.

14 X. Song, C. Wang, J. Chen, S. Xin, D. Yuan, Y. Wang, K. Dong, L. Yang, G. Wang, H. Zhang and S. Zhang, Unraveling the Synergistic Coupling Mechanism of Li^+ Transport in an ''Ionogel-in-Ceramic'' Hybrid Solid Electrolyte for Rechargeable Lithium Metal Battery, *Adv. Funct. Mater.*, 2022, **32**, 2108706.

15 Y. Su, X. Zhang, C. Du, Y. Luo, J. Chen, J. Yan, D. Zhu, L. Geng, S. Liu, J. Zhao, Y. Li, Z. Rong, Q. Huang, L. Zhang, Y. Tang and J. Huang, An All-Solid-State Battery Based on Sulfide and PEO Composite Electrolyte, *Small*, 2022, **18**, 2202069.

16 S. Liu, W. Liu, D. Ba, Y. Zhao, Y. Ye, Y. Li and J. Liu, Filler-Integrated Composite Polymer Electrolyte for Solid-State Lithium Batteries, *Adv. Mater.*, 2023, **35**, 2110423.

17 S. Kundu and Y. Ein-Eli, A review on design considerations in polymer and polymer composite solid-state electrolytes for solid Li batteries, *J. Power Sources*, 2023, **553**, 232267.

18 R. Chen, Q. Li, X. Yu, L. Chen and H. Li, Approaching Practically Accessible Solid-State Batteries: Stability Issues Related to Solid Electrolytes and Interfaces, *Chem. Rev.*, 2020, **120**, 6820–6877.

19 Y. Teng, H. Liu, Q. Wang, Y. He, Y. C. Hua, C. Li and J. Bai, In-doped $Li_7La_3Zr_2O_{12}$ nanofibers enhances electrochemical properties and conductivity of PEO-based composite electrolyte in all-solid-state lithium battery, *J. Energy Storage*, 2024, **76**, 109784.

20 A. Parejiya, R. Amin, M. B. Dixit, R. Essehli, C. J. Jafta, D. L. Wood, III and I. Belharouak, Improving contact impedance via electrochemical pulses applied to lithium–solid electrolyte interface in solid-state batteries, *ACS Energy Lett.*, 2021, **6**, 3669–3675.

21 S. Yuan, Y. Luo, X. Wang, C. Yao, K. Xia, J. Xiao, X. Fang, G. Jiang, J. Xiong and M. Fan, A novel composite solid electrolyte based on chemical bonding and physical reinforcing for all-solid-state lithium metal batteries, *J. Energy Storage*, 2024, **90**, 111853.

22 A. Jetybayeva, D. S. Aaron, I. Belharouak and M. M. Mench, Critical review on recently developed lithium and non-lithium anode-based solid-state lithium-ion batteries, *J. Power Sources*, 2023, **566**, 232914.

23 L. He, J.-H. Cao, Y.-K. Wang and D.-Y. Wu, Flexible ''polymer-in-ceramic'' composite solid electrolyte PI–$PEO_{0.2}$–PDA@$LATP_{0.8}$ and its ionic conductivity, *Energy Adv.*, 2022, **1**, 1028.

24 S. Wang, A. L. Monaca and G. P. Demopoulos, Composite solid-state electrolytes for all solid-state lithium batteries: progress, challenges and outlook, *Energy Adv.*, 2025, **4**, 1.

25 R. Sahore, Z. Du, X. C. Chen, W. B. Hawley, A. S. Westover and N. J. Dudney, Practical considerations for testing polymer electrolytes for high-energy solid-state batteries, *ACS Energy Lett.*, 2021, **6**, 2240–2247.

26 M. Ferreira, R. Schmidt, F. Xu, S. Ketabi, M. Cai and Y. Zhu, Polydopamine-Based Polymer Layer for Enhanced Interfacial Properties of Hybrid Ceramic−Polymer Solid Electrolytes, *ACS Appl. Energy Mater.*, 2023, **6**, 12095.

27 K. Pan, L. Zhang, W. Qian, X. Wu, K. Dong, H. Zhang and S. Zhang, A Flexible Ceramic/Polymer Hybrid Solid Electrolyte for Solid-State Lithium Metal Batteries, *Adv. Mater.*, 2020, **322**, 000399.

28 J. Yin, X. Xu, S. Jiang, H. Wu, L. Wei, Y. Li, J. He, K. Xi and Y. Gao, High ionic conductivity PEO-based electrolyte with 3D framework for dendrite-free solid-state lithium metal batteries at ambient temperature, *Chem. Eng. J.*, 2022, **431**, 133352.

29 Y.-Y. Sun, Q. Zhang, L. Fan, D.-D. Han, L. Li, L. Yan and P.-Y. Hou, Engineering the interface of organic/inorganic composite solid-state electrolyte by amino effect for all-solid-state lithium batteries, *J. Colloid Interface Sci.*, 2022, **628**, 877–885.

30 D. Cai1, D. Wang, Y. Chen, S. Zhang, X. Wang, X. Xia and J. Tu, A highly ion-conductive three-dimensional LLZAO-PEO/LiTFSI solid electrolyte for high-performance solid-state batteries, *Chem. Eng. J.*, 2020, **394**, 124993.

31 L. Chena, Y. Lib, S.-P. Lia, L.-Z. Fana, C.-W. Nanc and J. B. Goodenough, PEO/garnet composite electrolytes for solid-state lithium batteries: From ''ceramic-in-polymer'' to ''polymer-in-ceramic, *Nano Energy*, 2018, **46**, 176–184.

32 Y. Su, F. Xu, Y. Qiu, J. Zhang, X. Zhang and H. Wang, Electrolyte based on laser-generated nano-garnet in poly(ethylene oxide) for solid-state lithium metal batteries, *Chem. Eng. J.*, 2022, **443**, 136418.

33 C. Yang, Q. Wu, W. Xie, X. Zhang, A. Brozena, J. Zheng, M. N. Garaga, B. H. Ko, Y. Mao, S. He, Y. Gao, P. Wang, M. Tyagi, F. Jiao, R. Briber, P. Albertus, C. Wang, S. Greenbaum, Y.-Y. Hu, A. Isogai, M. Winter, K. Xu, Y. Qi and L. Hu, Copper-coordinated cellulose ion conductors for solid-state batteries, *Nature*, 2021, **598**, 590.

34 F. Baskoro, H. Q. Wong and H.-J. Yen, Strategic Structural Design of a Gel Polymer Electrolyte toward a High Efficiency Lithium-Ion Battery, *ACS Appl. Energy Mater.*, 2019, **2**, 3937.

35 D. M. Pesko, K. Timachova, R. Bhattacharya, M. C. Smith, I. Villaluenga, J. Newman and N. P. Balsara, Negative Transference Numbers in Poly(ethylene oxide)-Based Electrolytes, *J. Electrochem. Soc.*, 2017, **164**, E3569.

36 X. Zheng, T. Yang, J. Wei, C. Wang and M. Chen, Co-contribution of quenching and nanocrystallization on ionic-conductivity improvement of a composite electrolyte of polyethylene Oxide/$Li_7La_3Zr_2O_{12}$ nanofibers at 45 °C for all-solid-state Li metal batteries, *J. Power Sources*, 2021, **496**, 229843.

37 L. Gao, B. Tang, H. Jiang, Z. Xie, J. Wei and Z. Zhou, Fiber-Reinforced Composite Polymer Electrolytes for Solid-State Lithium Batteries, *Adv. Sustainable Syst.*, 2022, **6**, 2100389.

38 J. Yin, X. Xu, S. Jiang, H. Wu, L. Wei, Y. Li, J. He, K. Xi and Y. Gao, High ionic conductivity PEO-based electrolyte with 3D framework for dendrite-free solid-state lithium metal batteries at ambient temperature, *Chem. Eng. J.*, 2022, **431**, 133352.

39 Y. Zhao, J. Yan, W. Cai, Y. Lai, J. Song, J. Yu and B. Ding, Elastic and well-aligned ceramic LLZO nanofiber based electrolytes for solid-state lithium batteries, *Energy Storage Mater.*, 2019, **23**, 306.

40 Y. Su, F. Xu, Y. Qiu, J. Zhang, X. Zhang and H. Wang, Electrolyte based on laser-generated nano-garnet in poly(ethylene oxide) for solid-state lithium metal batteries, *Chem. Eng. J.*, 2022, **443**, 136418.

41 Z. Wan, D. Lei, W. Yang, C. Liu, K. Shi, X. Hao, L. Shen, W. Lv, B. Li, Q.-H. Yang, F. Kang and Y.-B. He, Low Resistance–Integrated All-Solid-State Battery Achieved by $Li_7La_3Zr_2O_{12}$ Nanowire Upgrading Polyethylene Oxide (PEO) Composite Electrolyte and PEO Cathode Binder, *Adv. Funct. Mater.*, 2019, **29**, 1805301.

42 D. Cai, D. Wang, Y. Chen, S. Zhang, X. Wang, X. Xia and J. Tu, A highly ion-conductive three-dimensional LLZAO-PEO/LiTFSI solid electrolyte for high-performance solid-state batteries, *Chem. Eng. J.*, 2020, **394**, 124993.

43 P. Pan, M. Zhang, Z. Cheng, L. Jiang, J. Mao, C. Ni, Q. Chen, Y. Zeng, Y. Hu and K. Fu, Garnet ceramic fabric-reinforced flexible composite solid electrolyte derived from silk template for safe and long-term stable All-Solid-State lithium metal batteries, *Energy Storage Mater.*, 2022, **47**, 279–287.

44 T. Li, X.-Z. Yuan, L. Zhang, D. Song, K. Shi and C. Bock, Degradation Mechanisms and Mitigation Strategies of Nickel-Rich NMC-Based Lithium-Ion Batteries, *Electrochem. Energy Rev.*, 2020, **3**, 43.

45 C. Li, Y. Xie, N. Zhang, L. Ai, Y. Liang, K. Tuo, X. Ye, G. Jia and S. Li, Optimization of $LiFePO_4$ cathode material based on phosphorus doped graphite network structure for lithium ion batteries, *Ionics*, 2019, **25**, 927–937.

46 H.-J. Noh, S. Youn, C. S. Yoon and Y.-K. Sun, Comparison of the structural and electrochemical properties of layered $Li[Ni_xCo_yMn_z]O_2$ (x = 1/3, 0.5, 0.6, 0.7, 0.8 and 0.85) cathode material for lithium-ion batteries, *J. Power Sources*, 2013, **233**, 121.

47 S.-U. Woo, C. S. Yoon, K. Amine, I. Belharouak and Y.-K. Sun, Significant Improvement of Electrochemical Performance of AlF_3-Coated $Li[Ni_{0.8}Co_{0.1}Mn_{0.1}]O2$ Cathode Materials, *J. Electrochem. Soc.*, 2007, **154**, A1005–A1009.

48 S. S. Zhang, J. Chen and C. Wang, Elemental Sulfur as a Cathode Additive for Enhanced Rate Capability of Layered Lithium Transition Metal Oxides, *J. Electrochem. Soc.*, 2019, **166**, A487–A492.